Review of Scientific Instruments

Line-imaging velocimetry for observing spatially heterogeneous mechanical and chemical responses in plastic bonded explosives during impact

Cite as: Rev. Sci. Instrum. **84**, 083903 (2013); https://doi.org/10.1063/1.4817307
Submitted: 06 March 2013 . Accepted: 18 July 2013 . Published Online: 12 August 2013

C. A. Bolme, and K. J. Ramos

View Online

Export Citation

CrossMark

ARTICLES YOU MAY BE INTERESTED IN

Line-imaging velocimeter for shock diagnostics at the OMEGA laser facility
Review of Scientific Instruments **75**, 4916 (2004); https://doi.org/10.1063/1.1807008

Laser interferometer for measuring high velocities of any reflecting surface
Journal of Applied Physics **43**, 4669 (1972); https://doi.org/10.1063/1.1660986

Accuracy and precision in photonic Doppler velocimetry
Review of Scientific Instruments **81**, 053905 (2010); https://doi.org/10.1063/1.3429257

AIP Publishing

© 2013 AIP Publishing LLC.

Line-imaging velocimetry for observing spatially heterogeneous mechanical and chemical responses in plastic bonded explosives during impact

C. A. Bolme[a] and K. J. Ramos
Shock and Detonation Physics, Los Alamos National Laboratory, Los Alamos, New Mexico 87545, USA

(Received 6 March 2013; accepted 18 July 2013; published online 12 August 2013)

A line-imaging velocity interferometer was implemented on a single-stage light gas gun to probe the spatial heterogeneity of mechanical response, chemical reaction, and initiation of detonation in explosives. The instrument is described in detail, and then data are presented on several shock-compressed materials to demonstrate the instrument performance on both homogeneous and heterogeneous samples. The noise floor of this diagnostic was determined to be 0.24 rad with a shot on elastically compressed sapphire. The diagnostic was then applied to two heterogeneous plastic bonded explosives: 3,3′-diaminoazoxyfurazan (DAAF) and PBX 9501, where significant spatial velocity heterogeneity was observed during the build up to detonation. In PBX 9501, the velocity heterogeneity was consistent with the explosive grain size, however in DAAF, we observed heterogeneity on a much larger length scale than the grain size that was similar to the imaging resolution of the instrument. © *2013 AIP Publishing LLC*. [http://dx.doi.org/10.1063/1.4817307]

I. INTRODUCTION

Spatial heterogeneity plays a pivotal role in the mechanical and chemical responses of a wide range of materials to high velocity impact. For energetic materials specifically, microstructural features affect localized material yielding and hydrodynamic flow, creating hot spots for detonation initiation. In this context, small changes in void content ($\Delta\rho/\rho$ = 0.2% in PBX 9501),[1] the type and percentage of plastic binder,[2] and the orientation and inherent defect content of energetic, molecular crystals[3] all have measurable effects on the sensitivity of the material to initiation. Identifying the many sources of heterogeneity and separating their contributions to hot spot initiation within plastic bonded explosive (PBX) microstructures is extremely challenging and requires more information than provided by the prototypical shock diagnostics currently in use. Surface velocimetry and magnetic particle velocity embedded gauges are examples of two diagnostics that have been used successfully for studying shock-to-detonation initiation behavior.[1] Combined, they are particularly well suited for determining unreacted shock and particle velocity Hugoniot points, measuring particle velocity profiles that quantify reactive wave evolution, and determining distance-to-detonation points (pop-plots).[4] In order to advance the understanding of detonation initiation from the continuum level to the material microstructure scale, spatially resolved diagnostics are necessary. Line-imaging and two-dimensional imaging extensions of diagnostics, such as velocity interferometer system for any reflector (VISAR) that have been very successful in the past, are promising avenues for observing microstructure-level response.

VISAR was developed over 40 years ago[5] and has become a standard technique for probing shocked materials. The optically-resolved variation of VISAR, or optically-recording velocity interferometer system (ORVIS), was demonstrated a decade later[6] and was further developed for line-imaging.[7] Line-imaging VISAR has become a common diagnostic at facilities that perform laser-driven shock and plasma physics experiments, but its use has remained quite limited within the gas gun community despite the successful demonstration of its utility.[8] The design and implementation of line-imaging VISAR as a routine diagnostic on gas guns is important because gas guns can offer different strain rate and loading conditions than lasers and can sustain pressures for much longer times than laser drives, allowing the study of different phenomena, such as granular compaction or the slow build-up to detonation in plastic bonded explosives.

We have implemented a line-imaging VISAR on a single stage gas gun to investigate heterogeneity during shock-to-detonation initiation and reactive wave evolution in energetic materials. The necessity for keeping the interferometer and experimenters remote from the gun during firing and the size scales and heterogeneity associated with measurements makes fielding line-imaging VISAR challenging. This instrument was specifically developed to be efficiently fielded on gas guns, and other facilities for remote firing of explosives, and to be insensitive to deleterious, light intensity variations inherently associated with velocity heterogeneity exhibited by PBX. The single stage gun is located in close proximity to a two-stage gun, indoor firing chamber, and a suite of other shock/detonation diagnostics. In this explosive area, the line-imaging VISAR can be fielded simultaneously with the other diagnostics to complement continuum measurements with ones on the microstructural level. This work details the implementation of the line-imaging VISAR diagnostic on the gas gun along with the associated data analysis. This instrument was used to observe a homogeneous elastic shock response in *c*-cut sapphire, from which the noise floor of the diagnostic was determined. The instrument was also applied to two different PBXs that exhibit more and less heterogeneity in their impact response. Instrument details and shot data are

[a]Author to whom correspondence should be addressed. Electronic mail: cbolme@lanl.gov

 © 2013 AIP Publishing LLC

presented along with a discussion of methods for maintaining consistent light intensity for data with significant heterogeneity.

II. EXPERIMENT

A. Line-imaging VISAR design and operation

The line-imaging VISAR system was designed similarly to the systems in place at the University of Rochester's Omega laser facility[9] and Lawrence Livermore National Laboratory's Jupiter Laser Facility. The beam from a 5 W Nd:YVO_4 continuous wave laser (Coherent Verdi) operating with a wavelength of 532 nm was sent through a 2 mm diameter polymer core multimode fiber. The fiber provided mode mixing of the laser through its 10 m length, which served to spatially homogenize the beam intensity and randomize the laser speckle pattern. A 5 mW 532 nm laser diode was positioned near the 5 W probe laser and could be directed into the optical fiber using a flip mirror as depicted in Fig. 1. All set up and alignment was performed with the 5 mW laser until directly before the shot, at which time the 5 W laser was used. The low power laser diode reduced laser safety requirements and facilitated the ease of setup and alignment of the target, especially since the lasers and detectors resided in a room separate from the target chamber. Due to the use of the multi-mode fiber to transport the laser light to the target chamber, no alignment changes were necessary when switching between the 5 mW and 5 W lasers.

The fiber transported the beam into the neighboring room that contained the catch tank and target chamber of the gas gun. The light exited the fiber on a small breadboard adjacent to the target chamber of a single stage light gas gun equipped with a wrap-around breech and a 78 mm diameter launch tube. Two cylindrical lenses (10 mm and 50 mm focal lengths) collimated the beam out of the fiber. The beam was then directed via a turning mirror and a 50% beamsplitter through a

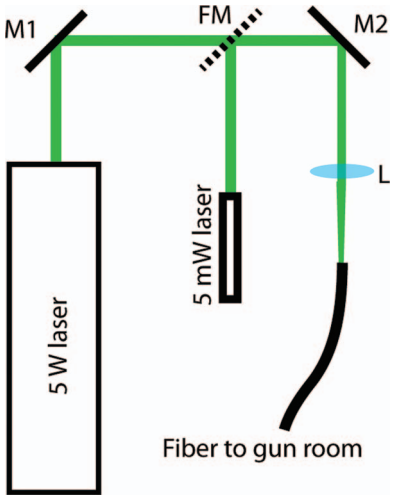

FIG. 1. Schematic of the probe laser injection into the 10 m long optical fiber. Two turning mirrors, M1 and M2, directed the beam into the fiber and a 250 mm focal length lens reduced the beam diameter to fit into the 2 mm diameter fiber. A flip mirror FM optionally directs a low power laser into the fiber for setup and alignment of the line-imaging VISAR diagnostic before the shot.

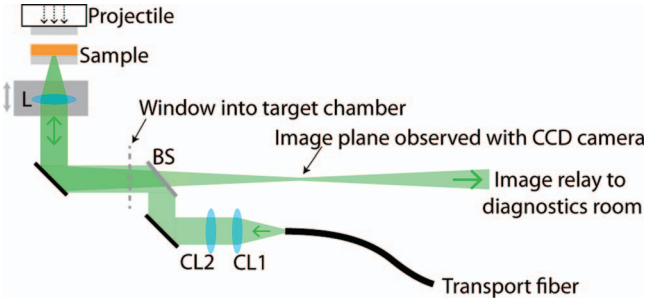

FIG. 2. Experimental layout of the line-imaging VISAR near the target. Cylindrical lenses, CL1 and CL2, collimated the laser light from the output of the fiber before it was reflected from a turning mirror and a 50:50 beamsplitter. A turning mirror in the catch tank directed the light normal to the sample surface. An f/4 lens imaged the target. The return light transited the same path but passed through the beamsplitter and an image of the target was created and then relayed to the interferometer.

532 nm anti-reflection coated window into the target chamber. An optical breadboard was fitted in the target chamber to facilitate easy positioning of the optics. A 2 in. diameter mirror directly in line with the gun barrel turned the beam so that it was incident normal to the target surface. Finally, the beam passed through a 2 in. diameter 200 mm focal length achromatic doublet lens, which served to image the light onto the target and to collect it after reflection.[10] The lens was mounted on a manual translation stage for easy adjustment of the lens position. The experimental layout is shown in Fig. 2. To reduce the amount of damage to the breadboard and translation stage, the optics were secured to the breadboard with nylon screws and mounted using posts made from phenolic rod. The only optics damaged in the shots were the final turning mirror and the achromatic lens, keeping the consumable parts to a modest cost for this diagnostic. The breadboard and translation stage typically received only minor damage in each shot and were therefore used in several shots before the degree of damage required that they be replaced.

After reflection from the target, the beam exited the target chamber along its incident path and then passed through the 50% beamsplitter. An image of the target surface was formed after the beamsplitter. A small CCD camera was positioned to flip into the beam path at this image plane to facilitate adjustment of the position of the imaging lens next to the target for best focus while observing small scratches in the reflective coating on the target. The image was relayed 4 m into the diagnostic room with 1:1 magnification, where it was collimated before being sent through a Mach-Zehnder (M-Z) interferometer as shown in Fig. 3. Due to the large thicknesses of the SF6 etalons used (130–202 mm) in the interferometer and the reduced laser coherence from transport through the fiber, the beam had to be collimated through the interferometer to achieve high contrast interference fringes. After the interferometer, the beam was imaged onto the 100 μm wide input slit of a streak camera (Optronis).

The interferometer contained 2 in. diameter optics, with protected silver mirrors for the two end mirrors and 50% partial reflectors for the two beamsplitters (CVI PR1-532-50-2025). The interferometer measured 0.92 m between the end mirrors and the angle between the two arms was 9.2°.

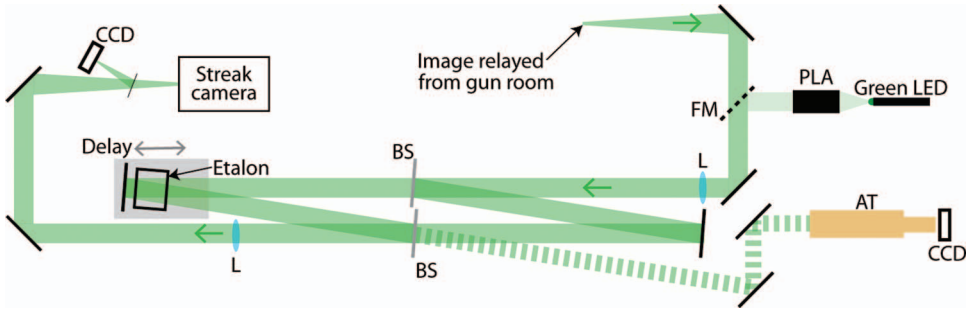

FIG. 3. Schematic of the interferometer and detector. The target image is relayed from the gun room, and then it is collimated to pass through the interferometer. The image was subsequently reformed on the entrance slit of the streak camera, which was monitored with a CCD camera. For alignment and adjustment of the white light fringes, a flip mirror, FM, was used to direct light from a green LED into the interferometer with the use of a photographic lens assembly, PLA. An alignment telescope, AT, and a CCD camera were used to align the interferometer optics and to optimize the white light fringes before the etalons were inserted into the interferometer.

Previous implementations of line-imaging VISAR on gas guns have used a wide-angle Michelson interferometer (WAMI) instead of an M-Z interferometer. In a WAMI, the interferometer has a single beamsplitter that is used first to split and then to recombine the beams. Using a single beamsplitter results in a slightly unbalanced interferometer since one of the paths does not pass through the beamsplitter but the other path passes through it twice. In the M-Z, each path transmits through one of the beamsplitters and reflects from the other, resulting in equivalent optical paths for each arm. The other advantage of using the M-Z is that the alignment is simplified by having separate beamsplitters for the splitting and recombination of the beams. Having separate optics allows changes in the fringe spacing (recombination angle) independently from the alignment of the beam reflected into and out of the interferometer.

The alignment of the optics in the interferometer was performed without the etalon inserted. The alignment was adjusted by imaging a reticle that was placed at the surface of each of the interferometer optics and was observed with an alignment telescope and CCD on the secondary output of the interferometer. A flip-in mirror directed the light from a green light emitting diode (LED) penlight into the interferometer, and the end mirror mounted on a motorized delay stage in the interferometer was scanned until interference fringes were observed. The extremely limited spatial and temporal coherence of the broadband LED source required high precision overlap of the two interferometer arms and required the two interferometer path lengths be equivalent to within $\sim 2\ \mu$m for fringes to be observed. While observing the interference of the green LED, the stationary end mirror and output beamsplitter were adjusted for the desired fringe period and orientation and for optimum fringe contrast.

Finally the desired etalons were inserted into the path on the motorized delay stage, and the stage was translated to increase the length of this arm by

$$d = h\left(1 - \frac{\cos\theta_{\mathrm{h}}}{n\cos\left(\sin^{-1}\left(\frac{\sin\theta_{\mathrm{h}}}{n}\right)\right)}\right), \tag{1}$$

where d is the distance, h is the etalon thickness, n is the refractive index of the etalon, and θ_{h} is the half-angle enclosed in the interferometer. The etalons and the path delay created a temporal delay τ between the two arms of the interferometer. This delay τ is given by (2),

$$\tau = \frac{2h}{c\cdot\cos\left(\sin^{-1}\left(\frac{\sin\theta_{\mathrm{h}}}{n}\right)\right)}\left(n - \frac{1}{n}\right), \tag{2}$$

where c is the speed of light. The cosine term in the denominator of (1) and (2) is a correction resulting from the angle of the light path through the etalons. Our resulting velocity per fringe (VPF_0) was given by

$$\mathrm{VPF}_0 = \frac{\lambda}{2\tau(1+\delta)}, \tag{3}$$

where λ is the wavelength of the probe light and δ is the chromatic dispersion of the etalons.[11] For the SF6 etalons that we used, the chromatic dispersion was 0.0942 at 532 nm.[12] The VPF_0 applies to free surfaces, however, a correction must be applied when observing the velocity of a reflecting surface through a window material due to the change in the refractive index of the window under shock compression. The VPF with the window correction is

$$\mathrm{VPF} = \frac{\mathrm{VPF}_0}{1+\frac{\Delta\nu}{\nu_0}}, \tag{4}$$

where $\Delta\nu/\nu_0$ is the VISAR correction factor.[13]

The target was illuminated over a 3 mm wide region, and the magnification of the target was 6.5 to the 100 μm wide slit of the streak camera. Using a resolution target positioned in the target chamber, we determined that the imaging resolution of the instrument was 27 μm. The temporal resolution was dependent on the sweep speed of the camera and the width of the input slit. The temporal resolution was 2.4 ns for the sapphire shot and 9.5 ns for the 3,3′-diaminoazoxyfurazan (DAAF) and PBX 9501 shots.

B. Gas gun experiments

The target configuration for the gas gun experiments is depicted in Fig. 4. For each of the samples, an optically polished window was vapor deposited with $\sim 0.6\ \mu$m of Al to provide a highly reflective surface. For the sapphire shot, the

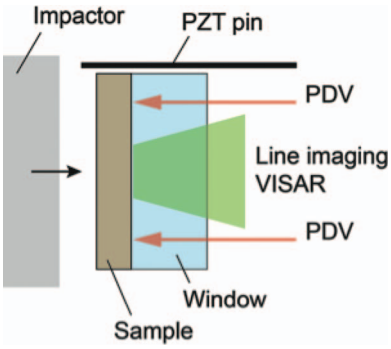

FIG. 4. Schematic of the target configuration showing the configuration of the velocity diagnostics and the PZT triggering pin.

projectile impacted the Al coated surface directly; whereas for the PBX 9501 and DAAF shots, the window was affixed to the explosive sample with a sub-micrometer layer of epoxy. The experiments are summarized in Table I.

Two to four photon Doppler velocimetry (PDV) probes were also fielded on the back surface of each sample, and the data were analyzed for comparison with the line-imaging VISAR velocities. The projectile velocity was measured, with an accuracy of ~0.1%, before impact using a laser beam interrupt method, and piezoelectric crush pins (Dynasen, Inc., Goleta, CA) were mounted flush or proud of the impact surface to provide an electronic timing signal to trigger the diagnostic instruments. The etalon thicknesses were selected such that the observed optical phase shift would be approximately 2.5 wave cycles. The number of integral phase wraps that occurred during the initial shock of the samples cannot be uniquely determined using only the line-imaging VISAR data. Both the PDV data and the projectile velocity were consulted to ensure that the data were adjusted for the correct number of 2π fringe jumps. These 2π jumps in phase were added at the point of largest phase discontinuity near the shock front and were added across 7 pixels in the temporal direction to account for the width of the input slit as it was relayed onto the CCD camera.

C. Data analysis

The spatial and temporal distortions (fisheye) in the streak records were corrected by mapping the distorted data from a second-order polynomial in each direction onto a grid with even spacing in the spatial and temporal dimensions. The interferogram from the sapphire shot is shown in Fig. 5(a). The interferograms were analyzed using the Fourier transform

TABLE I. Summary of experiment parameters.

Material			Sample thickness	Density	Impact velocity	Initial P
Impactor	Sample	Window	(mm)	(g/cm^3)	(m/s)	(GPa)
Sapphire	Sapphire		6.392	3.985	457.8	10.42
Sapphire	DAAF	PMMA[a]	6.353	1.684	630.4	3.37
6061 Al	PBX9501	PMMA[a]	4.007	1.833	830.9	3.95

[a]PMMA: Type 2 Rohm and Haas UVA.

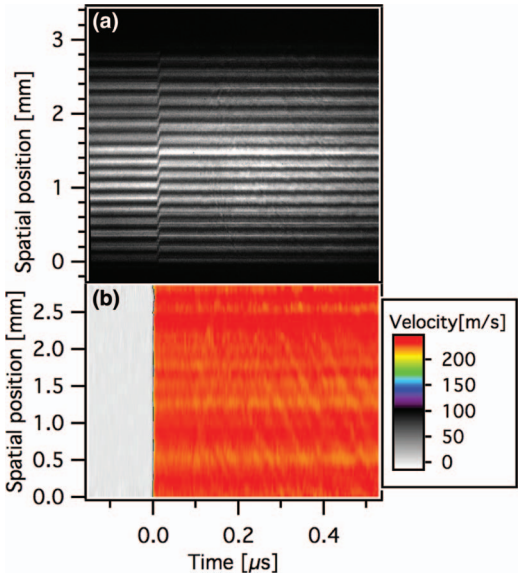

FIG. 5. (a) Interferogram for symmetric sapphire impact of 10.42 GPa. (b) Interface velocity of sapphire data shown in (a) as a function of spatial position along the sample.

method of Takeda,[14] which has been extensively implemented in interferometry analysis (see articles that cite Ref. 14 for relevant examples). The power spectrum obtained by discrete Fourier transform of the interferogram is shown in Fig. 6, with the frequency region that was selected for back transforming denoted by the dashed box. The optical phase shift that was extracted from the interferogram was multiplied by the VPF to yield the velocity as shown in Fig. 5(b).

III. RESULTS AND DISCUSSION

A. Sapphire

As line-imaging VISAR had not been previously fielded on this gun and because we are interested in observing the spatial heterogeneity of reacting explosives, we performed an experiment to establish the noise level of the diagnostic. Optically polished *c*-cut sapphire windows were used in a symmetric impact configuration with a projectile velocity of 457.8 m/s. This velocity resulted in a purely elastic response

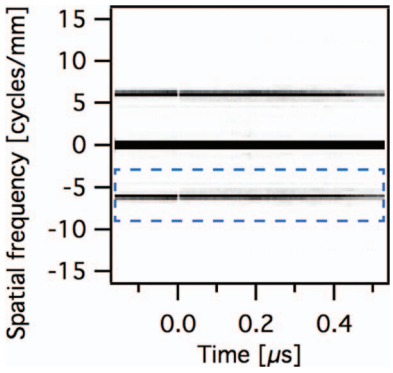

FIG. 6. Power spectrum from the discrete Fourier transform of the interferogram shown in Fig. 5(a). The dashed box shows the area which was selected for FFT analysis.

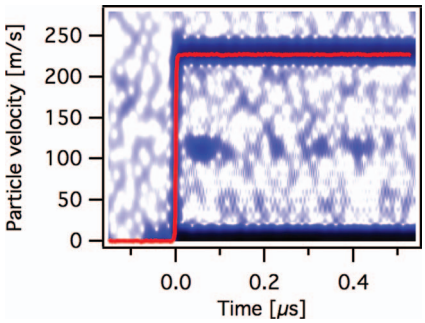

FIG. 7. Particle velocity for symmetric sapphire experiment. The intensity plot shows the analyzed PDV data and the red line shows the average of the data from the line-imaging VISAR.

in the sapphire (see Ref. 13 and references therein) with a particle velocity wave that we believe to be spatially smoother than the line-imaging VISAR could resolve. Fig. 5(a) shows the interferogram after the streak camera distortion was corrected and Fig. 5(b) shows the analyzed spatial velocity map of the elastic wave in sapphire. The etalons selected provided a VPF_0 of 142.6 m/s, which resulted in a VPF of 80.05 m/s after the sapphire window correction was applied.[15] The particle velocity of the shocked sapphire was 227.7 m/s with a standard deviation of 3 m/s (or 0.24 rad). With the assumption that the elastic wave in sapphire has less spatial heterogeneity than can be resolved with this line-imaging VISAR, we established the noise floor of the diagnostic to be 0.24 rad.

We compared the spatially averaged velocity measured with line-imaging VISAR to the velocity of the sapphire impactor and to the velocity measured by the PDV. Using the impactor velocity of 457.8 m/s, the observed particle velocity should be 229 m/s. The PDV probe yielded a velocity of 230.3 m/s. The PDV data and the spatially averaged line-imaging VISAR data are shown in Fig. 7. Comparison of the three velocity measurements shows that they differ by only 1.1%.

B. Heterogeneous reaction in plastic bonded explosives

Relative heterogeneity of reaction was examined in two different plastic bonded explosive formulations. These formulations were DAAF that was pressed with 5% Kel-F 800 binder and PBX 9501, which is a plastic bonded explosive formulation consisting of 95% octahydro-1,3,5,7-tetranitro-1,3,5,7-tetrazocine (HMX), 2.5% estane, and 2.5% bis(2,2-dinitropropyl)acetal/bis(2,2-dinitropropyl) (BDNPA-F). The input pressures and sample thicknesses were chosen to produce waves at the windowed surfaces that were partially run up to detonation.

The distortion-corrected interferograms and spatial velocity maps for the partial reaction in DAAF and in PBX 9501 are shown in Figs. 8 and 9, respectively. The DAAF data show velocity variations of approximately 3× the noise limit (0.24 rad = 7.7 m/s), and the magnitude of the variation was higher just behind the shock front arrival than it was at the peak velocity. The PBX 9501 velocity data show much larger velocity variations of approximately 10× the

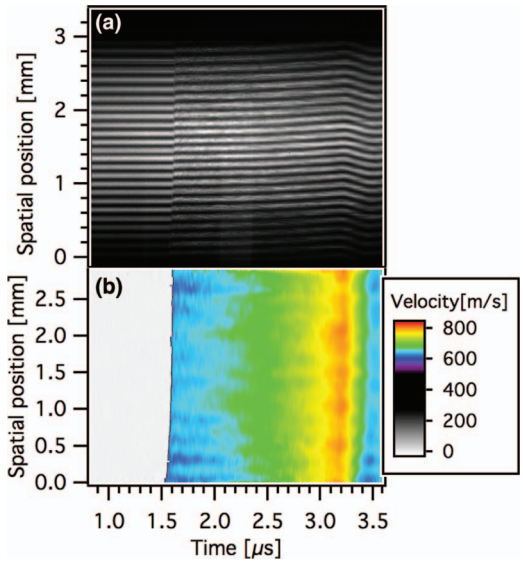

FIG. 8. (a) Interferogram of partial reaction in DAAF after impact of 3.37 GPa and transit through 6.353 mm of DAAF. (b) Interface velocity from DAAF data shown in (a) as a function of spatial position along the sample.

noise limit (0.24 rad = 8.6 m/s) with increasing variation at the peak velocity. (The noise limits differed between the two measurements because different etalon thicknesses, and therefore different velocity sensitivities, were used.) The material grain sizes and the velocity variations immediately after shock arrival and at the peak particle velocity are shown in Table II.

Velocity data was also collected from the PDV for these shots, and the data are shown in Figs. 10 and 11 and are overlaid with the spatially averaged velocity from the line-imaging VISAR. From these data, it is shown that the velocities from the PDV and the line-imaging VISAR are in good agreement,

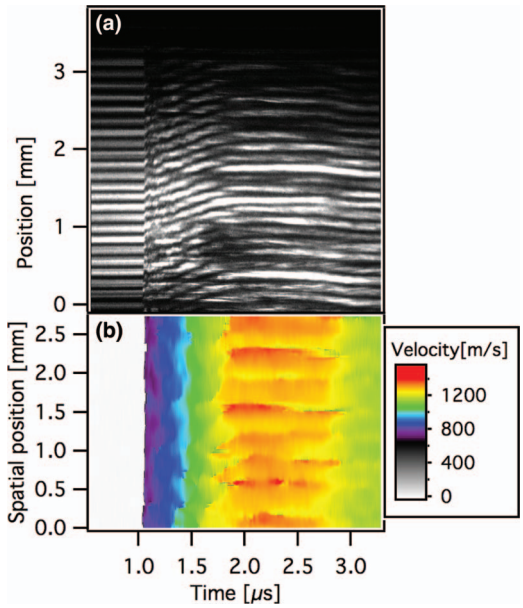

FIG. 9. (a) Interferogram of partial reaction in PBX 9501 after impact of 3.95 GPa and transit through 4.007 mm of PBX 9501. (b) Interface velocity from PBX9501 data shown in (a) as a function of spatial position along the sample.

TABLE II. Velocity heterogeneity starting 10 ns after arrival of the shock front and at the peak velocity. The velocity data was averaged for 10 ns at each of the times to obtain the spatial variation of the velocity.

		10 ns after shock arrival		At peak velocity	
Material	Mean grain size (μm)	Velocity variation (m/s)	Average period of velocity variation (μm)	Velocity variation (m/s)	Average period of velocity variation (μm)
DAAF	38	37	300	25	260
PBX 9501	147–234 (Ref. 16)	79	290	93	310

but the PDV does not capture the spatial velocity variation during the build up to detonation.

The DAAF shot shows observable curvature at shock breakout. The tilt of the projectile at impact was measured as 0.6 mrad, yet the variation in the breakout timing across the line-imaging velocimetry is consistent with 12 mrad of tilt, which is significantly greater than can be accounted for by the non-planarity of the DAAF sample. Closer examination of the shock breakout timing shows that the variation is better described as curvature than as linear tilt, and an additional shot on DAAF at lower pressure also shows similarly shaped curvature. The variation in density of a different sample of DAAF was determined by dicing and measuring immersion density, and we observed variations in density up to 0.5% between ~0.125 cm^3 sections of a single pressed piece. Therefore, we believe that the observed variation in breakout timing in DAAF was due to the density variations in the sample. Density variations in PBX 9501 half as large as we measured in DAAF were shown to have a measurable effect on the PBX 9501 pop-plot.[1] We expect the density variations in DAAF could have significant implications for its detonation initiation.

C. Data comparison and assessment

The experiments on DAAF and PBX 9501 show spatial velocity variation during the reaction build up to detonation that is significantly larger than the noise level of the diagnostic, suggesting heterogeneous chemical reaction and detonation initiation. Additionally, the power spectrum of the PBX 9501 interferogram in Fig. 12 shows additional spatial frequency peaks that correspond to periods of 190 and 280 μm. The similarity between these periods and the grain size of the crystallites in the sample leads to the supposition that the reaction heterogeneity stems from the variation in shock response of individual crystals or from hot spot initiation arising from voids between crystals.

A similarity between the grain size and the observed spatial period of the velocity heterogeneity was not present in the DAAF data. This result could be because the 38 μm grain size of the DAAF crystals was comparable to the 27 μm resolution of the instrument, which might mask the velocity heterogeneity arising from the grains, or because the smaller grains of the DAAF do not provide a large enough run distance to develop more significant velocity variations. Instrument spatial resolution relative to the size of microstructure features is an important consideration for spatially resolved investigations. Future studies with this instrument will explore correlations between the spatially heterogeneous response and the sample microstructure directly under the line imaging velocimetry.

One of the difficulties in quantifying the spatial velocity variations is the inability to completely separate the phase shift information that is proportional to velocity from the spatial intensity variations in illumination. Ideally, the target illumination and the intensity of the reflected light would be spatially even throughout the experiment. In actuality, there are spatial variations in the intensity of the detected light that

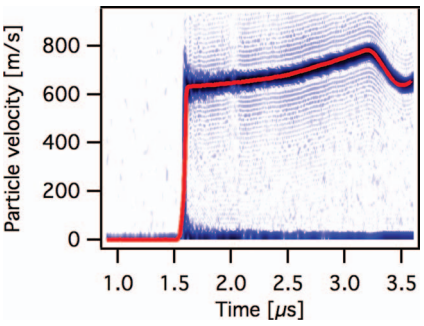

FIG. 10. Particle velocity for partial reaction in DAAF. The intensity plot shows the analyzed PDV data and the red line shows the average of data from the line-imaging VISAR.

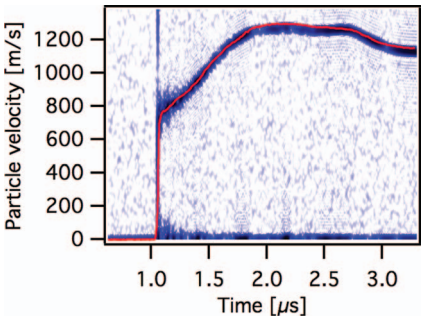

FIG. 11. Particle velocity for partial run to detonation in PBX 9501. The intensity plot shows the analyzed PDV data and the red line shows the average of the data from the line-imaging VISAR.

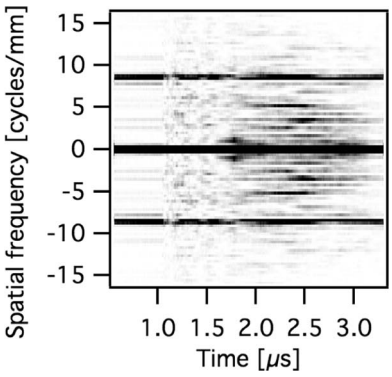

FIG. 12. Power spectrum from the discrete Fourier transform of the PBX 9501 interferogram shown in Fig. 9(a). The velocity heterogeneity is apparent in the additional frequencies that develop with increasing reaction.

cannot be fully separated from the fringe movement. These spatial variations in intensity are most obvious in the PBX 9501 interferogram in Fig. 9(a). The mottled appearance of this interferogram arises from the velocity variations causing localized curvature of the reflective surface, which redirected the probe light outside of the collection angle of the target imaging lens. These variations in intensity are an inherent difficulty of spatially resolved investigations and experimental compensation has to be made for the effects of heterogeneity on illumination, commensurately. This instrument maintained relatively even intensity throughout the experiments despite the pronounced heterogeneity exhibited by PBX 9501. The following experimental details were key to this success and should not be overlooked: a specular coating on our sample windows, a multimode fiber which served to spatially homogenize the beam intensity and randomize the laser speckle pattern, and an appropriately large numerical aperture lens located close to the reflecting sample plane. Often times, diffuse surfaces are used for VISAR experiments to homogenize light return from samples and to maintain light levels when the shock roughens the surface of the reflector. However, preparatory roughening of the reflector surface is undesirable for line-imaging VISAR experiments because the heterogeneity in scuffed, diffuse reflective coatings is convoluted with the heterogeneous response of the sample. Instead of roughening the reflector surface, we opted to use the multimode fiber, which served to condition the beam intensity and speckle and to maintain the reflected signal intensity after shock arrival at the specular window coating. In selecting the numerical aperture of the imaging lens, we balanced the desire for a large acceptance angle that would capture signal from the heterogeneously curving sample surface with the desire to probe the sample at normal incidence and with a depth-of-focus that would permit imaging of the moving sample interface. An additional option to further divorce the variations in signal intensity from the variations in sample velocities, albeit at significantly increased experimental complexity, would be to employ a quadrature detection technique as commonly used in VISAR[17] and 2D VISAR.[18]

IV. SUMMARY

In summary, we have described the implementation of a line-imaging VISAR on a single stage gas gun including the design and operation, data analysis, and the demonstration of the spatial and velocity resolution. This instrument was specifically developed to overcome challenges fielding line-imaging VISAR efficiently during remote firing of explosives and the deleterious effects of spatial heterogeneity exhibited by PBX on velocity data. Experimental results using this instrument to investigate spatial heterogeneity in the impact and initiation response of several PBXs and *c*-cut sapphire were reported. The symmetric impact of sapphire in the elastic regime, demonstrated a 0.24 rad noise floor for the instrument. Both PBXs exhibited distinct heterogeneity above this level. For PBX 9501, grains were spatially resolved and the pronounced heterogeneity varied periodically on a similar scale. For DAAF, the observed velocity variations were not commensurate with the grain size, indicating that larger scale microstructural features must be contributing to initiation. These results illustrate the importance of spatially resolved diagnostics to understanding impact, initiation, and detonation behavior at the microstructural level. Future work will use the line-imaging VISAR to further investigate these observations on PBXs and on explosive single crystals.

ACKNOWLEDGMENTS

The authors would like to thank Dr. Peter Celliers, Dr. David Erskine, and Dr. Rick Gustavsen for participating in helpful discussion, Tim Pierce, Adam Pacheco, and Ben Hollowell for their assistance in fielding the experiments, and Elizabeth Francois for providing the DAAF PBX. This work was performed at Los Alamos National Laboratory and was funded by the National Nuclear Security Administration Science Campaign 2 (High Explosives Science). Los Alamos National Laboratory is operated by Los Alamos National Security, LLC, for the National Nuclear Security Administration of the U.S. Department of Energy under Contract No. DE-AC52-06NA25396.

[1]R. L. Gustavsen, S. A. Sheffield, R. R. Alcon, and L. G. Hill, paper presented at the 12th International Symposium on Detonation, San Diego, CA, 11–16 August 2002 (unpublished).
[2]R. L. Rabie and H. H. Harry, Los Alamos National Laboratory Report No. LA-UR-92-1928; R. L. Gustavsen, S. A. Sheffield, R. R. Alcon, L. G. Hill, R. E. Winter, D. A. Salisbury, and P. Taylor, AIP Conf. Proc. **505**, 879–882 (1999); L. G. Green, R. J. Wasley, and P. E. Kramer, Lawrence Radiation Laboratory Report No. UCRL-50851, 1970.
[3]J. J. Dick, R. N. Mulford, W. J. Spencer, D. R. Pettit, E. Garcia, and D. C. Shaw, J. Appl. Phys. **70**(7), 3572 (1991).
[4]R. Engelke and S. A. Sheffield, in *Encyclopedia of Applied Physics* (VCH Publishers, Inc., 1993), Vol. 6, p. 327.
[5]L. M. Barker and R. E. Hollenbach, J. Appl. Phys. **43**(11), 4669 (1972).
[6]D. D. Bloomquist and S. A. Sheffield, J. Appl. Phys. **54**(4), 1717 (1983).
[7]W. F. Hemsing, A. R. Matthews, R. H. Warnes, M. J. George, and G. R. Whittemore, in *Proceedings of the American Physical Society Topical Conference on Shock Compression of Condensed Matter – 1991* (North Holland, 1992), p. 767.
[8]W. M. Trott, M. R. Baer, J. N. Castaneda, L. C. Chhabildas, and J. R. Asay, J. Appl. Phys. **101**(2), 024917 (2007).
[9]P. M. Celliers, D. K. Bradley, G. W. Collins, D. G. Hicks, T. R. Boehly, and W. J. Armstrong, Rev. Sci. Instrum. **75**(11), 4916 (2004).
[10]The f/4 imaging lens collected light at an angle of 7° from normal incidence. The correction to the velocity measurement due to this fast optic would be 0.4% for a free surface measurement. The correction is less because the spread in the collection angle was reduced due to the higher refractive index of the windows on the samples. For these windowed samples, the correction was <0.2% and was neglected. [D. H. Dolan, Report No. SAND2006-1950, 2006].
[11]L. M. Barker and K. W. Schuler, J. Appl. Phys. **45**(8), 3692 (1974).
[12]*Optical Glass Data Sheets* (Schott North America, 2012).
[13]L. M. Barker and R. E. Hollenbach, J. Appl. Phys. **41**(10), 4208 (1970).
[14]M. Takeda, H. Ina, and S. Kobayashi, J. Opt. Soc. Am. **72**(1), 156 (1982).
[15]B. J. Jensen, D. B. Holtkamp, P. A. Rigg, and D. H. Dolan, J. Appl. Phys. **101**(1), 013523 (2007).
[16]C. B. Skidmore, D. S. Phillips, S. F. Son, and B. W. Asay, in *Shock Compression of Condensed Matter - 1997*, edited by S. C. Schmidt, D. P. Dandekar, and J. W. Forbes (American Institute of Physics, Melville, 1998), Vol. 429, pp. 579.
[17]W. F. Hemsing, Rev. Sci. Instrum. **50**(1), 73 (1979).
[18]P. M. Celliers, D. J. Erskine, C. M. Sorce, D. G. Braun, O. L. Landen, and G. W. Collins, Rev. Sci. Instrum. **81**(3), 035101 (2010); D. J. Erskine, R. F. Smith, C. A. Bolme, P. M. Celliers, and G. W. Collins, *ibid.* **83**(4), 043116 (2012).